Quantification of left ventricular strain and torsion by joint analysis of 3D tagging and cine MR images

Ezgi Berberoğlu, Christian Stoeck, Sebastian Kozerke, Martin Genet

▶ **To cite this version:**

Ezgi Berberoğlu, Christian Stoeck, Sebastian Kozerke, Martin Genet. Quantification of left ventricular strain and torsion by joint analysis of 3D tagging and cine MR images. Medical Image Analysis, 2022, 10.1016/j.media.2022.102598 . hal-03604931

HAL Id: hal-03604931
https://hal.science/hal-03604931v1

Submitted on 10 Mar 2022

HAL is a multi-disciplinary open access archive for the deposit and dissemination of scientific research documents, whether they are published or not. The documents may come from teaching and research institutions in France or abroad, or from public or private research centers.

L'archive ouverte pluridisciplinaire **HAL**, est destinée au dépôt et à la diffusion de documents scientifiques de niveau recherche, publiés ou non, émanant des établissements d'enseignement et de recherche français ou étrangers, des laboratoires publics ou privés.

Quantification of left ventricular strain and torsion by joint analysis of 3D tagging and cine MR images

Ezgi Berberoğlu[a,b,c], Christian T. Stoeck[a], Sebastian Kozerke[a], and Martin Genet[b,c,*]

[a]*Institute for Biomedical Engineering, University and ETH Zurich, Zurich, Switzerland*
[b]*Laboratoire de Mécanique des Solides (LMS), École Polytechnique/C.N.R.S./Institut Polytechnique de Paris, Palaiseau, France*
[c]*MΞDISIM team, Inria, Palaiseau, France*

Abstract

Cardiovascular magnetic resonance (CMR) imaging is the gold standard for the non-invasive assessment of left-ventricular (LV) function. Prognostic value of deformation metrics extracted directly from regular cine CMR images has been shown by numerous studies in the clinical setting, but with some limitations to detect torsion of the myocardium. Tagged CMR introduces trackable features in the myocardium that allow for the assessment local myocardial deformation, including torsion; it is, however, limited in the quantification of radial strain, which is a decisive metric for assessing the contractility of the heart. In order to improve cine-only and tagged-only approaches, we propose to combine the advantages of both image types by fusing global shape motion obtained from cine images with the local deformation obtained from tagged images. To this end, tracking is first performed on cine images, and subsequently, the resulting motion is utilized to mask and track tagged data. Our implementation is based on a recent finite element-based motion tracking tool with mechanical regularization. Joint cine and tagged images registration performance is assessed based on deformation metrics including LV strain and twist using human and in-house porcine datasets. Results show that joint analysis of cine and 3DTAG images provides better quantification of LV strain and twist as either data source alone.

Keywords—Cardiac magnetic resonance imaging, 3D tagging, Image registration, Finite element method.

1. Introduction

Cardiovascular magnetic resonance (CMR) is considered the reference standard for the assessment of healthy and diseased myocardium (Alfakih et al., 2004). Quantification of global cardiac function is widely performed based on left-ventricular ejection fraction (LVEF), stroke volume, or myocardial thickness. Despite their common usage for the assessment of cardiac performance, relying on global measures alone may result in misinterpretation of cardiac performance (Abraham et al., 2001). Compared to global contractile properties, regional changes have been found to serve better for diagnosis and early intervention in many cardiac diseases (Hunter et al., 2012; Ibrahim, 2011; Nagueh et al., 2001; Ng et al., 2011; Sutherland et al., 1994). Among them, ischemic heart diseases are known to cause local dysfunctions of the heart wall while global functional measures remain insensitive to the location and severity of the infarction (Collins, 2015; Friedberg et al., 2009).

* Corresponding author.
E-mail address: martin.genet@polytechnique.edu (Martin Genet).

Moreover, regional changes in cardiac function are proposed to be a strong indicator of both hypertrophic cardiomyopathy (HCM) (Huang et al., 2017; Serri et al., 2006; Smiseth et al., 2016) and heart failure with preserved LVEF (Hasselberg et al., 2015; Smiseth et al., 2016).

Cine CMR has become one of the clinical work horses to assess the global functional parameters such as ventricular volumes, LVEF and mass (Castillo et al., 2003). It provides excellent temporal (Barkhausen et al., 2001; Plein et al., 2001) and spatial resolutions, with a higher signal-to-noise ratio and tissue contrast than other imaging modalities (Barkhausen et al., 2001; Pereles et al., 2001). However, material point tracking from cine CMR is challenging due to the lack of contrast within the myocardium (Wu et al., 2014). Beyond cine imaging, CMR tagging has been introduced to quantify local deformation measures, e.g., strain and torsion (Rademakers et al., 1997; Stuber et al., 1999) by introducing the non-invasive physical markers on the myocardium (Zerhouni et al., 1988), which is followed by a more efficient and fast technique, SPAtial Modulation of Magnetization (SPAMM) (Axel et al., 1989). The tag fading problem inherent to SPAMM was solved introducing complementary SPAMM (CSPAMM) (Fischer et al., 1993), which was later added the capability to track three-dimensional (3D) deformation of the heart with the slice-following CSPAMM (Fischer et al., 1994). More recent improvements in 3D tagging techniques have been focused on the misregistration issues related to multi-slice acquisitions and decreasing the acquisition time (Rutz et al., 2008; Stoeck et al., 2012). Other than cine and tagged MRI, displacement encoding with stimulated echoes (DENSE) allows for a direct visualization of myocardial deformation encoded into the MR signal phase (Kim et al., 2004) and demonstrated to allow the quantification of LV function both on animals (Haggerty et al., 2013, 2014) and in the clinical setting (Bilchick et al., 2014).

Studies on the healthy human heart using CMR tagging have reported regional differences in strain distribution (Bogaert et al., 2001; Moore et al., 2000; Young et al., 1994). Although CMR tagging provides regional deformation metrics, the saturation bands generated in the image make it impossible to accurately delineate the endocardial and epicardial borders (Makram et al., 2016). Given its image quality, a robust assessment of LV functional analysis remains challenging (Schrauben et al., 2018). Therefore, the patient needs to be scanned separately for the cine and tagged CMR, increasing both the scan time and number of breath-holds (Schrauben et al., 2018). Alternative methods to CMR tagging such as CMR feature tracking (FT) (Pedrizzetti et al., 2011) were developed to speed up the existing techniques for clinical feasibility. CMR-FT is similar to speckle tracking echocardiography (STE) (Bohs et al., 2000) in terms of its dependence on tracking epicardial and endocardial borders and has been validated against tagged harmonic phase (HARP) analysis for the assessment of peak average circumferential myocardial strain (Hor et al., 2010) and used in diagnosing cardiac disorders (Hor et al., 2010; Schuster, Paul, et al., 2013). However, radial strain obtained from this method is not satisfying (Padiyath et al., 2013). Limited to 2D acquisitions (Schuster et al., 2011), strain measurements obtained from CMR- FT techniques are dependent on the delineation of the endocardial and epicardial contours by the user, leading to limited inter-study reproducibility (Morton et al., 2012) and intra-observer reproducibility (Schuster, Morton, et al., 2013). Among other strain components, only the global circumferential strain agrees with CMR tagging results (Cowan et al., 2015). However, the segmental

differences cannot be characterized unless tagging is utilized (Augustine et al., 2013; Cowan et al., 2015).

The finite element model (FEM)-based registration technique used in this study has already been tested and validated both on in-vivo (Genet et al., 2018) and synthetic MR images (Berberoğlu et al., 2019), and also for the LV torsion quantification in case of impaired LV function (Castellanos et al., 2021). We further demonstrated that limitations of radial strain quantification from 3DTAG images can be related to limited spatial resolution and signal-to-noise ratio (SNR) (Berberoğlu et al., 2021). Therefore, we propose an alternative way to improving strain quantification from 3DTAG data here based on joint analysis of cine and tagged CMR to combine the advantages of 3DTAG and cine MR images. The manuscript is organized as follows. We first describe the image dataset and the FEM-based image registration technique in Section 2. Section 3 outlines the analysis results. After a detailed discussion in Section 4, Section 5 concludes with some important remarks.

2. Materials and methods

In this section, we first describe the image datasets used in this study and the FEM-based image registration technique is later summarized. Next, the processing pipeline to couple cine and tagged images is explained. The section concludes with the introduction of metrics used to assess the performance of joint analysis of cine and tagged CMR data, which is referred to as m3DTAG hereafter.

2.1. Image acquisition and preprocessing

Two datasets are used to demonstrate the performance of the proposed m3DTAG image registration technique. The first one includes 32 image sets retrospectively selected from our previous porcine study (Stoeck et al., 2021). In brief, imaging was performed on a 1.5T clinical Philips Achieva MR system (32-channel cardiac receiver array). All animal handling procedures and protocols were approved by the Cantonal Veterinary Office (Zurich, Switzerland). The imaging protocol consisted of multi-slice cine CMR in short-axis view with the following parameters: 1.8x1.8 mm^2 spatial resolution, 8 mm slice thickness, 25 heart phases, 1.5ms/3ms TE/TR as well as 3D tagged imaging (Rutz et al., 2008) acquiring three stacks with orthogonal CSPAMM (Fischer et al., 1993) using the following imaging parameters: 2x2x5 mm^3 spatial resolution,110x110x110 mm^3 field-of-view, 26 heart phases, 4mm tagline distance, 4.3ms/9.2ms TE/TR, turbo factor 3, echo planar imaging (EPI) factor 7.

The second dataset consists of volunteer data from the Cardiac Motion Analysis Challenge (Tobon-Gomez et al., 2013), which is publicly available. The dataset includes cine and 3DTAG images of healthy volunteers. In this study, we excluded five of the volunteers (V4, V5, V7, V8, and V11) due to poor image segmentation quality or slice inter breath-hold misalignment. For both the porcine and human datasets, cine and 3DTAG images were normalized to their maximum pixel intensity and spatially resampled by Lanczos interpolation to obtain an isotropic pixel size using MeVisLab[1].

[1] http://www.mevislab.de

2.2. FEM-based image registration

Though the image coupling strategy described in Section 2.3 is mostly independent from the choice of image registration technique, we now briefly describe the FEM-based image registration technique used in this study, which was detailed in (Genet et al., 2018). It requires an initial volume mesh that matches the heart phase from which the registration starts. To this end, left-ventricular geometries were obtained from the manual segmentation of the porcine dataset, based on the cine images at end-systole (ES) using MeVisLab[1]. Segmentation was performed both on the short-axis and long-axis views. The resulting surface meshes were converted into volume meshes using first-order finite elements using GMSH (Geuzaine et al., 2009). The local transmural, circumferential and longitudinal directions were assigned to each node and element on the LV mesh with respect to the centroid using the normalized pseudo-prolate spheroidal coordinate system (Genet et al., 2014, 2015). For the human dataset, the LV geometries at end-diastolic frames were readily available along with cine and 3DTAG images. In accordance to the previous studies, we run the registration algorithm for the regularization strength β = 0.1, which has been found to be a near-optimal value for a wide range of images (Genet et al., 2018; Lee et al., 2019). For the registration of cine, 3DTAG and m3DTAG images, performed using the finite element method, the LV meshes were extruded by an extra layer of elements with a thickness ranging from 2 to 3 mm around the ventricle, referred to as boundary layer, generated using GMSH. FEM-based image registration utilized in this study is based on the pixel intensities within the mesh, therefore, an accurate tracking of an interface requires inclusion of pixels on both sides, which is solved for the epicardium by adding the boundary layer. Therefore, the purpose of the boundary layer is solely to improve the image registration performance and it is not considered for the strain computation (Genet et al., 2018).

For image registration, a continuum formulation and the discretization technique using the FE method is introduced. I_0 and I_t denote the scalar intensity fields for the images representing the object in the reference, Ω_0, and current, Ω_t, configurations, respectively. Between these two configurations, we can define a deformation map that translates the reference points $\boldsymbol{X} \in \Omega_0$ onto their spatial counterparts $\boldsymbol{x} = \boldsymbol{\Phi}(\boldsymbol{X}) = \boldsymbol{X} + \boldsymbol{U}(\boldsymbol{X}) \in \Omega_t$, through the displacement field, $\boldsymbol{U}$. The registration problem is to find the displacement field between Ω_0 and Ω_t. The task is intrinsically ill-posed due the presence of image noise. Hence, the problem is reformulated as a minimization problem:

$$\text{Find } \boldsymbol{U} = \text{argmin}\left\{ h = (1-\beta)\Psi^{\text{im}} + \beta\Psi^{\text{reg}} \right\}, \tag{1}$$

weighted by regularization strength β, the image similarity metric,

$$\psi^{\text{im}} = \frac{1}{2} \| I_t \circ \boldsymbol{\Phi} - I_0 \|^2_{L^2(\Omega_0)}, \tag{2}$$

and the regularization energy

$$\psi^{\text{reg}} = \frac{1}{2} \| \mathbf{div}(\boldsymbol{\sigma}) \|^2_{L^2(\Omega_t)}, \tag{3}$$

where $\boldsymbol{\sigma}$ is the Cauchy stress tensor. This registration technique has its novelty in utilizing a continuum finite strain formulation of the equilibrium gap principle introduced in (Claire et al., 2004), readily discretizable with standard finite elements. The main advantage of utilizing the equilibrated warping is that it enforces strong mechanical sense to the displacement field without imposing any constraint on the strain magnitude and depends solely on the balance of mechanical equilibrium. The use of finite elements also provides geometrical regularization through the FE mesh.

The classical Ciarlet-Geymonat potential is used to model the strain energy potential

$$\rho_0\,\psi = \frac{\kappa}{2}\left(J^2 - 1 - \ln(J)\right) + \frac{\mu}{2}\left(I_C - 3 - 2\ln(J)\right), \tag{4}$$

in terms of bulk and shear modulus, κ and μ, and the volume map, $J = \mathrm{Det}(\boldsymbol{F})$. The right Cauchy-Green deformation tensor is represented by $\boldsymbol{C} = \boldsymbol{F}^{\boldsymbol{T}}\boldsymbol{F}$, while $I_C = \mathrm{Tr}(\boldsymbol{C})$. The variational formulation of Equation (1) is obtained by following the general FE procedure, which is then linearized and discretized using standard continuous Lagrange elements. One can refer to (Genet et al., 2018) for more details on the formulation and solution procedure. The method is implemented based on FEniCS[2] and VTK libraries, and freely available as a Python library. (https://gitlab.inria.fr/mgenet/dolfin_warp).

2.3. Coupling SSFP and 3DTAG images

Figure 1 illustrates the pipeline to generate m3DTAG images. First, FEM-based image registration is performed on standard multi-slice balanced steady-state free precession (bSSFP) images (Figure 1.a). In order to mask the tagged images, the resulting displacement fields are linearly interpolated in time to match the temporal resolution of 3DTAG images according to:

$$\boldsymbol{d}^{\mathrm{m}}_{\mathrm{3DTAG}} = \boldsymbol{d}^{\mathrm{n}}_{\mathrm{SSFP}} + \left(\boldsymbol{d}^{\mathrm{n+1}}_{\mathrm{SSFP}} - \boldsymbol{d}^{\mathrm{n}}_{\mathrm{SSFP}}\right)\frac{\left(t^{\mathrm{m}}_{\mathrm{3DTAG}} - t^{\mathrm{n}}_{\mathrm{SSFP}}\right)}{\left(t^{\mathrm{n+1}}_{\mathrm{SSFP}} - t^{\mathrm{n}}_{\mathrm{SSFP}}\right)} \tag{5}$$

with $t^{\mathrm{n}}_{\mathrm{SSFP}}$ and $t^{\mathrm{n+1}}_{\mathrm{SSFP}}$ corresponding to the acquired heart phases of the bSSFP acquisition and $\boldsymbol{d}^{\mathrm{n}}_{\mathrm{SSFP}}$ and $\boldsymbol{d}^{\mathrm{n+1}}_{\mathrm{SSFP}}$ being the corresponding displacement fields. The initial reference mesh is mapped onto the 3DTAG images using the DICOM header information of slice position and angulation and subsequently warped using the interpolated displacement fields (Figure 1.b). Finally, 3DTAG images are masked using the meshes at each time frame and a background intensity is assigned to the masked region. The background intensity value, denoted γ, is defined as the average of the 95$^{\mathrm{th}}$ percentile of the image intensities, considering only the voxels covered by the LV wall. It represents the unique parameter of the coupling strategy, and its impact on the m3DTAG tracking is thoroughly studied in Section 3.1. The corresponding short-axis and long-axis views after masking are shown in Figure 1.c and Figure 1.d, respectively. m3DTAG image registration is then performed.

[2] https://www.fenicsproject.org

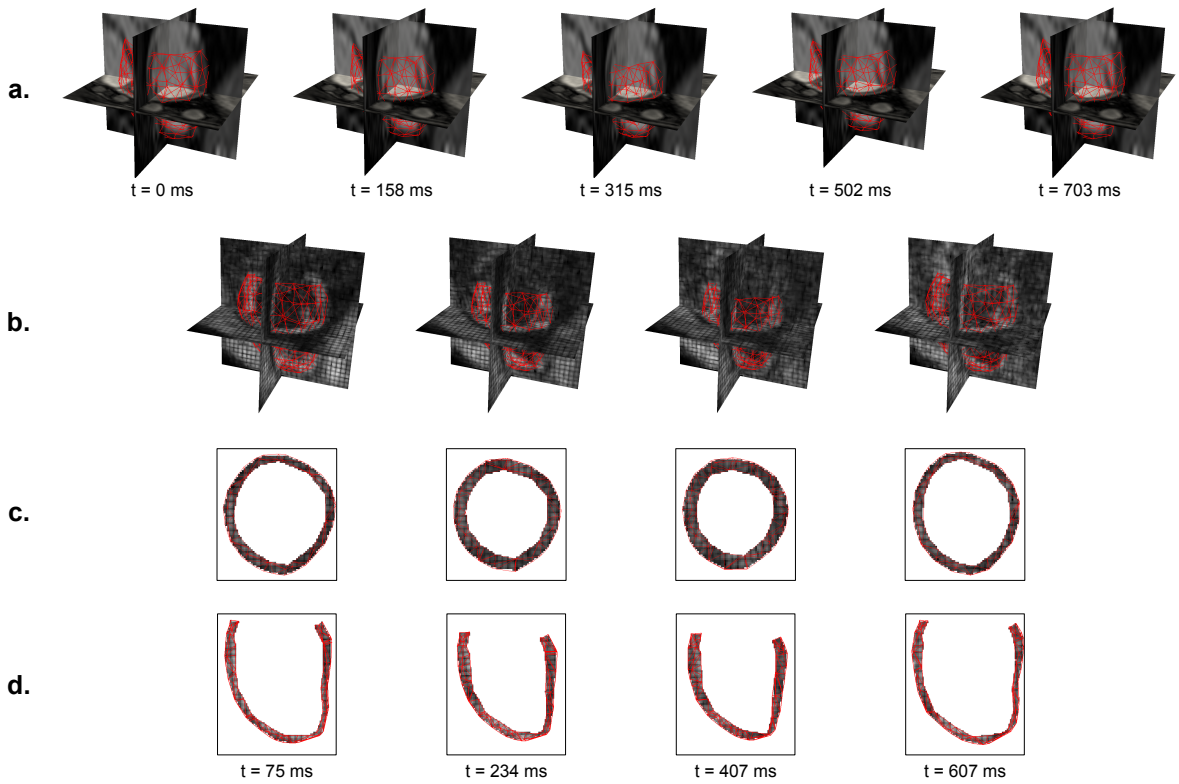

Figure 1 m3DTAG image generation pipeline. (a) Mesh configurations obtained from SSFP image registration, which are translated into 3DTAG image coordinates and interpolated in time to match the acquisition time for 3DTAG images, shown in (b) superimposed with 3DTAG images. m3DTAG images on short-axis (c), and long-axis (d) views, respectively. Masking is performed by keeping the tag line pattern inside the mesh, while the rest of the image intensity (background intensity) is assigned to a constant value.

2.4. Metrics used to assess m3DTAG image registration performance

FEM-based image registration is performed separately on SSFP, 3DTAG, and m3DTAG images. Performance of m3DTAG image registration is assessed for varying background intensities in terms of two deformation metrics. First the mean ± standard deviation of the Green-Lagrange strain error is reported. For this purpose, we define the component-wise Green-Lagrange strain error at ES with respect to ED:

$$e^{\mathrm{i}} = s^{\mathrm{i}} - s^{\mathrm{i}}_{\mathrm{SSFP}}, \tag{6}$$

where e^{i} is the strain error in s^{i}, that is the scalar strain value for component s over element i. Reference strains are obtained from SSFP images and represented by $s^{\mathrm{i}}_{\mathrm{SSFP}}$. ES Green-Lagrange strains are rotated in local pseudo-prolate spheroidal coordinates, and represented by the radial, circumferential, and longitudinal components. In this study, we utilized the P1 elements such that the strain is constant over each element. Therefore, the strain analysis was performed at the element level. The mean (e_{avg}) and standard deviation (e_{std}) in e^{i} are computed across the elements of a mid LV section for both the 3DTAG and m3DTAG images. For m3DTAG image registration, we compute the averaged e_{avg} and e_{std} over porcine/human datasets for a given background intensity.

The second performance metric is the mean ± standard deviation in maximum LV twist error. We first define the LV twist, $\Phi_{\mathrm{img}}^{\mathrm{t}}$, as the difference in rotations averaged through apical, $\boldsymbol{\alpha}_{\mathrm{img}}^{\mathrm{t,apex}}$, and basal regions, $\boldsymbol{\alpha}_{\mathrm{img}}^{\mathrm{t,base}}$, for img = 3DTAG, SSFP, m3DTAG at time frame t. The error in LV twist, e_{img}^{Φ}, is computed with respect to the 3DTAG image registration,

$$\Phi_{\mathrm{img}}^{\mathrm{t}} = \boldsymbol{\alpha}_{\mathrm{img}}^{\mathrm{t,apex}} - \boldsymbol{\alpha}_{\mathrm{img}}^{\mathrm{t,base}}, \tag{7}$$

$$e_{\mathrm{img}}^{\Phi} = \max\left|\Phi_{img}^{\mathrm{t}}\right| - \max|\Phi_{3DTAG}^{\mathrm{t}}|, \tag{8}$$

where $\max\left|\Phi_{\mathrm{img}}^{\mathrm{t}}\right|$ is the maximum LV twist over time. The mean ($e_{\mathrm{avg,img}}^{\Phi}$) and standard deviation ($e_{\mathrm{std,img}}^{\Phi}$) in e_{img}^{Φ} are computed across LV for SSFP and m3DTAG images. For a given background intensity, $e_{\mathrm{avg,img}}^{\Phi}$ and $e_{\mathrm{std,img}}^{\Phi}$ are averaged over the porcine/human datasets for the m3DTAG image analysis. We further computed the averaged normalized absolute error (%) in LV twist, $\Phi_{\mathrm{err,avg}}$, and strain components, $e_{\mathrm{err,avg}}$:

$$\Phi_{\mathrm{err,avg}} = \frac{1}{N_{\mathrm{case}}}\sum_{j=1}^{N_{\mathrm{case}}}\frac{\left|e_{\mathrm{img}}^{\Phi}\right|}{\max|\Phi_{3DTAG}^{\mathrm{t}}|}100\ (\%), \tag{9}$$

$$e_{\mathrm{err,avg}} = \frac{1}{N_{\mathrm{case}}}\sum_{j=1}^{N_{\mathrm{case}}}\frac{\sqrt{\sum_{i=1}^{N_{\mathrm{el}}}\left(s_{\mathrm{m3DTAG}}^{\mathrm{j,i}} - s_{\mathrm{SSFP}}^{\mathrm{j,i}}\right)^2}}{\max|s_{\mathrm{SSFP}}|}100\ (\%), \tag{10}$$

where $s_{\mathrm{m3DTAG}}^{\mathrm{j,i}}$ and $s_{\mathrm{SSFP}}^{\mathrm{j,i}}$ are the scalar strain values for m3DTAG and SSFP registrations for the j^{th} porcine/human dataset and i^{th} mesh element, respectively. N_{el} is the total number of elements in the mesh and N_{case} denotes the number of porcine/human datasets over which the normalized absolute error (%) is computed.

In order to compare the m3DTAG registration to the previous tracking challenge (Tobon-Gomez et al., 2013), we compute the normalized markers error, err, using the landmarks tracked by two observers on 3DTAG data and as published in (Tobon-Gomez et al., 2013), using following formula:

$$\mathrm{err} = \frac{1}{n_{\mathrm{markers}}}\sum_{m=1}^{n_{\mathrm{markers}}}\frac{\sum_{t=1}^{n_{\mathrm{frames}}}\left\|\underline{X}^{\mathrm{m}}(t) - \underline{X}^{\mathrm{m,GT}}(t)\right\|}{\sum_{\mathrm{t}=1}^{n_{\mathrm{frames}}}\left\|\underline{X}^{\mathrm{m,GT}}(t+1) - \underline{X}^{\mathrm{m,GT}}(t)\right\|}, \tag{11}$$

where n_{markers} and n_{frames} denote the number of valid markers within the mesh in the undeformed configuration and the number of time frames, respectively. $\underline{X}^{\mathrm{m,GT}}(f)$ stands for the reference/ground truth (GT) position of marker m while $\underline{X}^{\mathrm{m}}(t)$ is the tracked position at frame t.

3. Results

3.1. Analysis of method parameters

Figure 2 shows the mean ± standard deviations in maximum LV twist error (Figure 2.a) and component-wise ES Green-Lagrange strain errors (Figure 2.b-d) as a function of background intensity normalized by the 95th percentile of the image intensity. The performance assessment of LV twist quantification is performed relative to the results of 3DTAG image registration. The green region in Figure 2.a represents the error range in SSFP registration, which is -7.08 ± 3.65 and the red curve indicates for the mean ± standard deviation in LV twist error for m3DTAG registration. m3DTAG images perform better in terms of LV twist quantification in comparison to SSFP images for $\gamma < 1.6$, having the smallest error, -0.03 ± 0.82, when $\gamma = 0.4$.

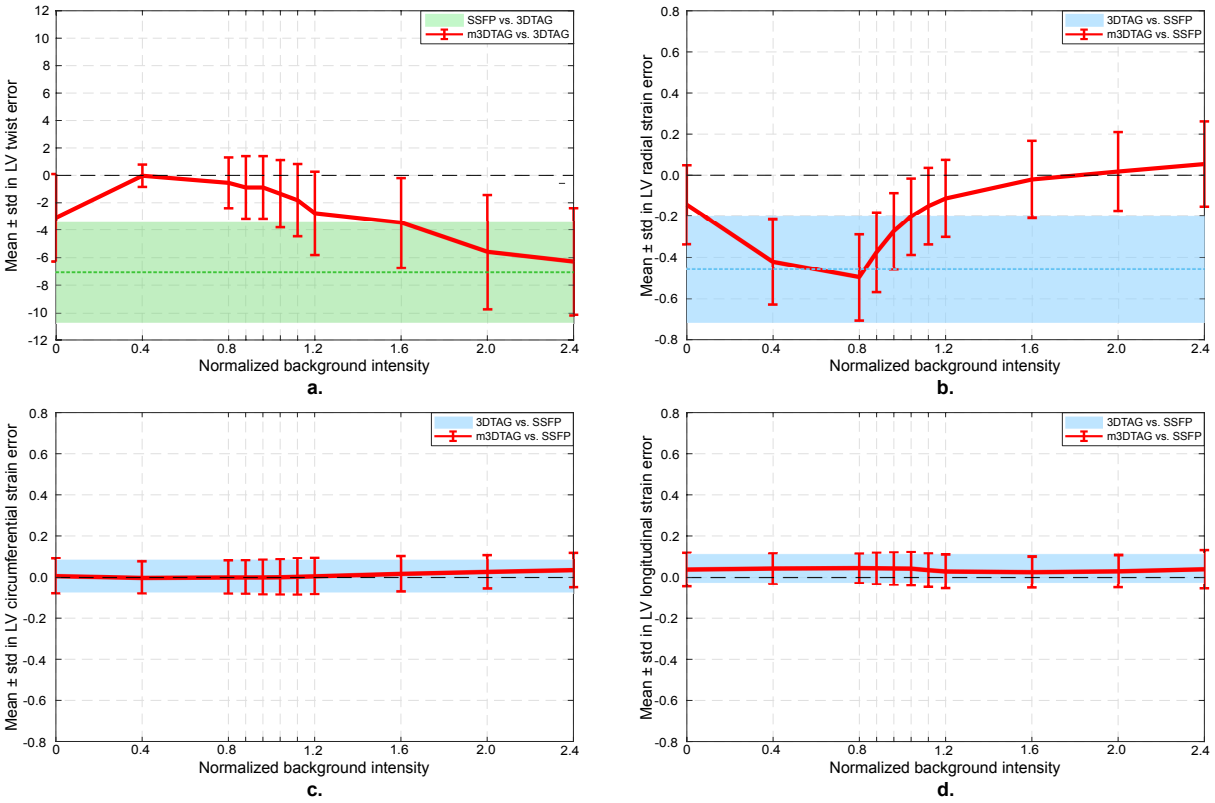

Figure 2 Effect of image background intensity on LV twist and strain error after masking of 3DTAG images. Mean ± standard deviation in LV twist error with respect to 3DTAG image registration, which is assumed to be the reference for the LV twist error computation (a). Red curve represents the error in m3DTAG registration. Green region represents the error in SSFP images, with the mean value shown by the green dotted line. Higher levels of background intensity results in larger errors in LV twist similar to SSFP. Mean ± standard deviation in radial strain error with respect to SSFP registration, which yields the reference strains for the strain error computation (b). Red curve represents the error in m3DTAG registration. Blue region represents the error in 3DTAG registration, with the mean value shown by the blue dotted line. For higher levels of background intensity, there is a decrease in error as m3DTAG tracking performs closer to SSFP tracking. The errors in circumferential (c) and longitudinal strains (d) (shown by the red lines for m3DTAG registration) are insensitive to a change in background intensity.

For strain, SSFP registration is considered the reference. The mean ± standard deviation in radial strain error (Figure 2.b) is 0.46 ± 0.26 for 3DTAG images, represented by the blue region, while the red curve stands for the error in m3DTAG registration. For $\gamma > 1.05$, m3DTAG images yield less error than 3DTAG images and

perform close to SSFP registration for $\gamma \in [1.6, 2.0]$. 3DTAG and m3DTAG registrations perform almost equally well for the circumferential (Figure 2.c) and longitudinal (Figure 2.d) strain quantification and the results are not sensitive to a change in background intensity.

In order to determine the "optimal" background intensity, γ^*, at which LV twist and radial strain are captured equally well, Figure 3 shows the averaged normalized absolute error (%) in LV twist (defined by Equation (9)), and Green-Lagrange strain components (defined by Equation (10)). The radial strain and the twist error depend on the background intensity while the circumferential and longitudinal strains remain insensitive. In principle, one can relate the optimal background intensity with the image signal only, independent of the scaling used. Based on the summation of errors in radial strain and twist, an "optimal" value is found at the minimum of 37.2 %, for $\gamma^* = 1.13$.

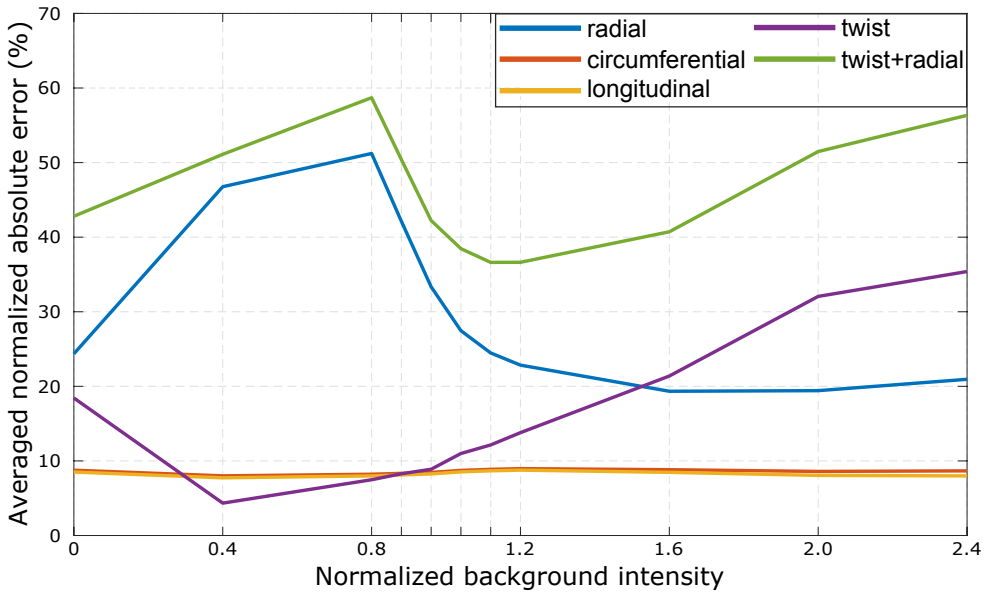

Figure 3 Determination of "optimal" image background intensity for m3DTAG analysis of porcine data. Averaged normalized absolute error (%) is plotted for LV twist, and Green-Lagrange strain components. LV twist and the radial strain are the two metrics that significantly vary with respect to image background intensity while the circumferential and longitudinal components remain insensitive. The summation of errors in twist and radial strain yields the optimal background intensity of 1.13, minimizing errors in these two metrics.

3.2. Method validation

After assigning the optimal background intensity, the joint registration technique presented in this paper is validated against the benchmark data of the Cardiac Motion Analysis Challenge (Tobon-Gomez et al., 2013). The performance of the image tracking algorithms was assessed relative to the manually tracked landmarks over 3DTAG images by two observers. Figure 4 shows the normalized marker errors computed using Equation (11) for all datasets from the challenge, for SSFP, 3DTAG and m3DTAG images (for $\gamma^* = 1.13$). Figure 4 shows the mean and standard deviation in normalized marker errors across all volunteers for FEM-based registration using SSFP, 3DTAG, and m3DTAG images as well as the challenge competitors, separated by the dashed line. m3DTAG image registration yields a normalized markers error of 1.39 ± 0.93. In case of SSFP image registration, it is 2.60 ± 0.64, 3.04 ± 0.64 and 2.48 ± 0.54 for FEM-based registration, INRIA, and UPF, respectively. The normalized

markers errors for 3DTAG image registration are 0.76 ± 0.33, 0.82 ± 0.31, 0.68 ± 0.23, 0.99 ± 0.56 and 0.80 ± 0.25 for FEM-based registration, INRIA, UPF, IUCL, and MEVIS, respectively.

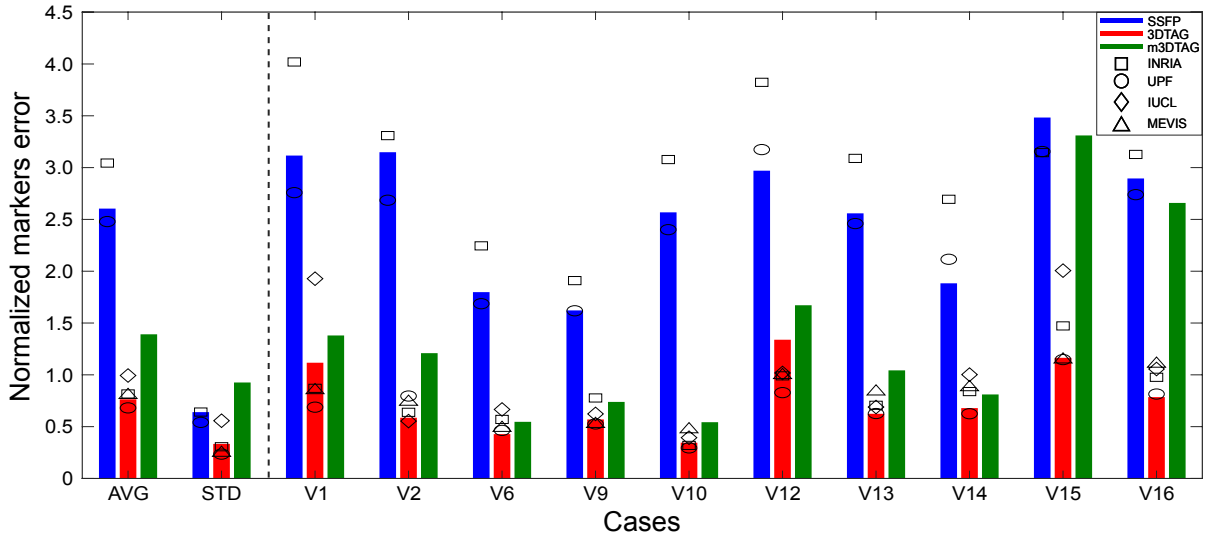

Figure 4 Validation of m3DTAG registration using Cardiac Motion Challenge data. Normalized markers errors for FEM-based registration using SSFP, 3DTAG, and m3DTAG images are represented by the blue, red, and green bar plots, respectively. The markers errors for other competitors (INRIA, UPF, IUCL and MEVIS) in the challenge are represented on top of the related bar plots. The average (AVG) and standard deviation (STD) in markers errors over all volunteers are separated by the dashed line. FEM-based registration performs well for all types of images, staying in the same normalized markers error range for the other groups.

3.3. Left ventricular strain and twist quantification

In Figure 5, we plotted the maximum LV twist for SSFP, 3DTAG and m3DTAG image registrations, using γ^* for each porcine dataset. The mean ± standard deviation (AVG) over all porcine datasets is represented by the first group of bar plots and the rest stands for the individual cases included in this study. On average, maximum LV twist for 3DTAG image registration is 11.05° ± 3.34°. SSFP registration yields an average maximum LV twist of 3.97° ± 2.04° while m3DTAG registration performs closer to 3DTAG registration with the LV twist value of 9.23° ± 2.59°. Figure 6 represents the ES Green-Lagrange strain components for SSFP, 3DTAG, and m3DTAG image registrations. For each component, mean ± standard deviation (AVG) in ES Green-Lagrange strains over all porcine datasets is represented as the first group of bar plots separated by a dashed line. The average ES radial strain for m3DTAG registration is 0.50 ± 0.20 while it is 0.20 ± 0.16 for 3DTAG and 0.65 ± 0.22 for SSFP image registrations (Figure 6.a). For the circumferential component, all types of images perform equally: the average ES strains are 0.14 ± 0.07, 0.14 ± 0.05 and 0.14 ± 0.07 for m3DTAG, 3DTAG and SSFP registrations, respectively (Figure 6.b). The average longitudinal strains are 0.14 ± 0.07, 0.13 ± 0.05 and 0.17 ± 0.04 for m3DTAG, 3DTAG and SSFP registrations, respectively (Figure 6.c). The pairwise t-test between the m3DTAG and SSFP registration yields the following p-values: $p_{\mathrm{rr}} < 0.05$, $p_{\mathrm{cc}} = 0.05$, $p_{\mathrm{ll}} < 0.05$ and $p_{\Phi} < 0.05$, for radial, circumferential, longitudinal strain components, and the twist, respectively. The p-values computed for m3DTAG and 3DTAG registrations are $p_{\mathrm{rr}} < 0.05$, $p_{\mathrm{cc}} = 0.73$, $p_{\mathrm{ll}} = 0.19$ and $p_{\Phi} < 0.05$.

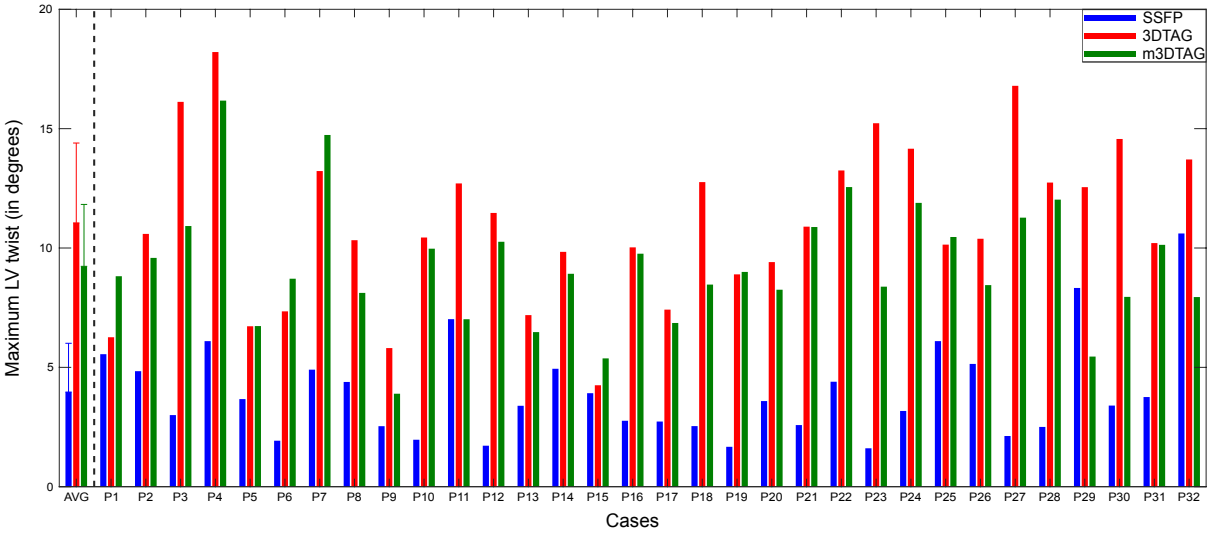

Figure 5 Maximum LV twist values for the porcine dataset. Blue, red, and green bars represent the max LV twists for SSFP, 3DTAG, and m3DTAG registrations, respectively. Mean ± standard deviation (AVG) in LV twist computed over all animals are separated by a dashed line. m3DTAG registration performs closer to 3DTAG registration in terms of LV twist quantification while SSFP yields comparably lower LV twist.

For the optimal background intensity, we performed Bland-Altman analysis to assess the agreement between SSFP, 3DTAG and m3DTAG registrations in terms of maximum LV twist and ES LV Green-Lagrange strain components, see Figure 7. For each plot, the 95% agreement interval is shown by the solid lines and the corresponding mean value by the dotted lines. Mean differences in max LV twist in SSFP and m3DTAG registrations with respect to reference 3DTAG registration are 7.09° and -1.82°, respectively (Figure 7.a). Mean differences in ES LV radial strain in 3DTAG and m3DTAG registrations with respect to reference SSFP registration are -0.457 and -0.151, respectively (Figure 7.b). For the circumferential component, 3DTAG and m3DTAG perform almost the same, with the respective mean errors 0.00447 and 0.00328 (Figure 7.c). The mean difference for longitudinal component is slightly larger for 3DTAG and m3DTAG registrations; 0.0428 and 0.0341, respectively (Figure 7.d).

Following the same approach as in the porcine data analysis, we run the registration algorithm on each image type; SSFP, 3DTAG, and m3DTAG for the Cardiac Motion Analysis Challenge data (Tobon-Gomez et al., 2013). Figure 8 shows the analysis results in terms of the maximum LV twist (Figure 8.a) and the component-wise ES Green-Lagrange strains (Figure 8.b-d). The mean and standard deviation (AVG) in LV twist over all the volunteers included in this study are 1.80° ± 1.31°, 12.5° ± 2.72° and 11.87° ± 3.79° for SSFP, 3DTAG and m3DTAG registrations, respectively, and separated by a dashed line (Figure 8.a). The averaged values (AVG) for all strain components are represented by the first group of bar plots (Figure 8.b-d). The averaged ES radial strains are 0.17 ± 0.15, -0.02 ± 0.10 and 0.16 ± 0.18 for SSFP, 3DTAG and m3DTAG images, respectively. SSFP and m3DTAG images performed equally well although 3DTAG registration yields negative radial strain. The averaged ES circumferential strains are 0.15 ± 0.06, 0.15 ± 0.07 and 0.14 ± 0.08 while the

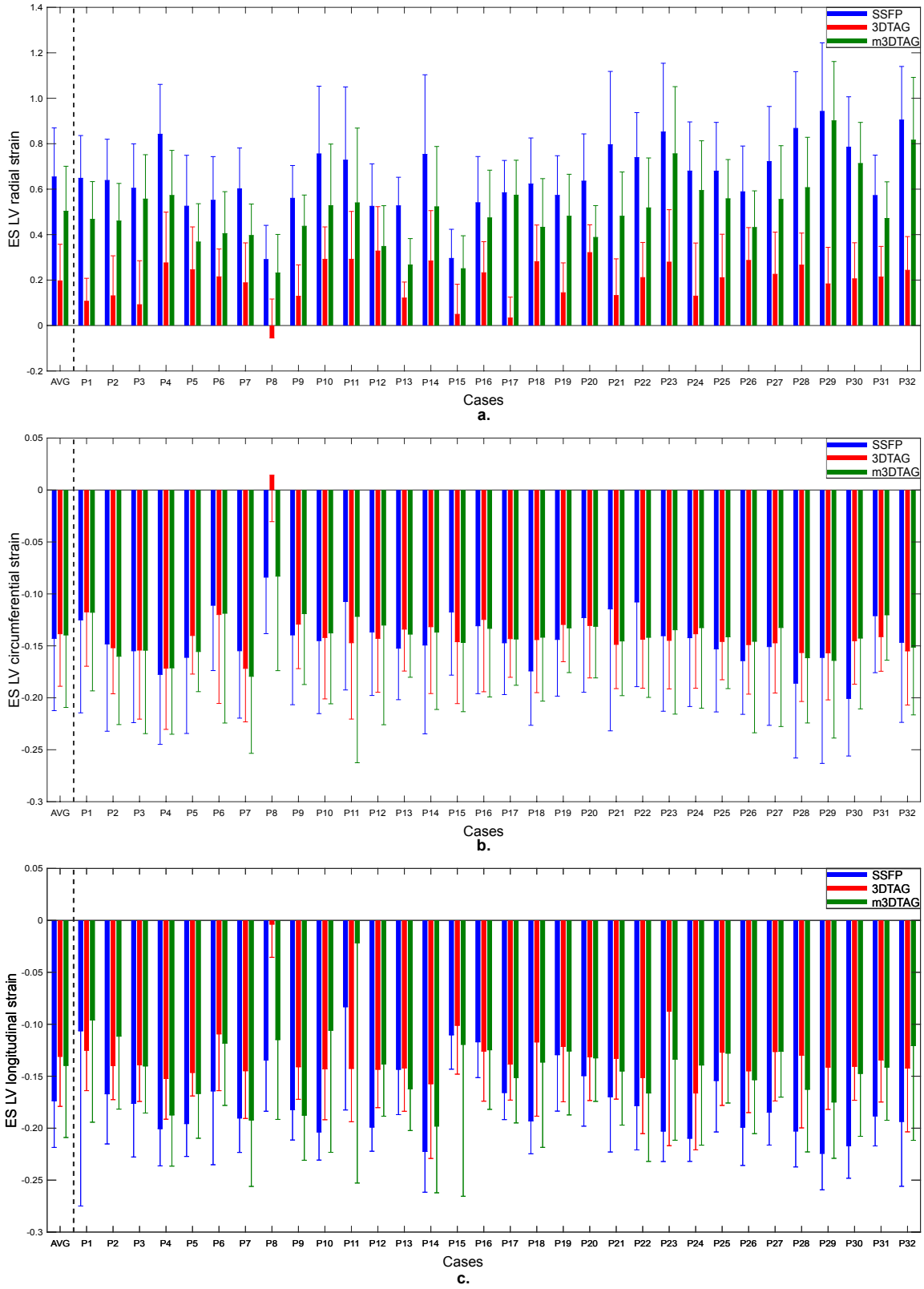

Figure 6 End-systolic Green-Lagrange strain components for the porcine dataset. Blue, red, and green bars represent the results for SSFP, 3DTAG, and m3DTAG registrations, respectively. Radial (a), circumferential (b) and longitudinal (c) strains are represented both for the averaged (AVG) values over all image sets (separated by a dashed line) and individual cases. On average, m3DTAG registration performs closer to SSFP registration in terms of radial strain quantification while circumferential and longitudinal strains are captured almost equally for any type of image.

longitudinal ones are 0.14 ± 0.07, 0.14 ± 0.06 and 0.12 ± 0.09 for SSFP, 3DTAG and m3DTAG registrations, respectively. The pairwise t-test between the m3DTAG and SSFP registration yields the following p-values for the strain components and the twist: $p_{\mathrm{rr}} = 0.74$, $p_{\mathrm{cc}} = 0.47$, $p_{\mathrm{ll}} = 0.44$ and $p_{\Phi} < 0.05$ while they are $p_{\mathrm{rr}} < 0.05$, $p_{\mathrm{cc}} = 0.35$, $p_{\mathrm{ll}} = 0.23$ and $p_{\Phi} = 0.48$ when m3DTAG and 3DTAG registrations are compared.

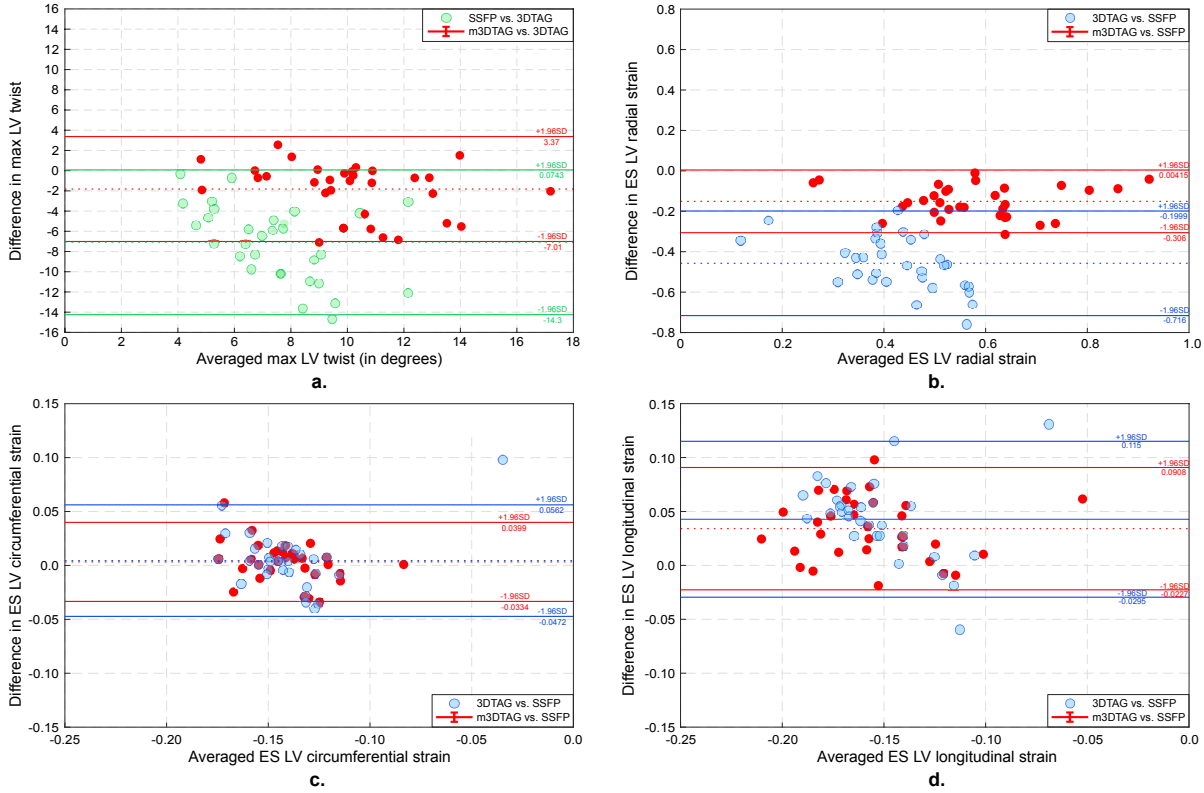

Figure 7 Bland-Altman analysis to assess the agreement between SSFP, 3DTAG and m3DTAG registrations for the optimal background intensity. The solid and dotted lines represent the 95% agreement interval and the mean difference, respectively, with the color code represented by the legend. Comparison of SSFP and m3DTAG registrations for max LV twist assessment with respect to 3DTAG registration (a). The absolute mean of the difference between m3DTAG and 3DTAG is smaller than the one between SSFP and 3DTAG with a smaller agreement interval. Comparison of 3DTAG and m3DTAG registrations for radial strain with respect to SSFP registration (b). m3DTAG registration underestimates the SSFP registration less than 3DTAG does with a relatively smaller agreement interval. For the circumferential (c) and longitudinal (d) components, both images yield similar errors with respect to SSFP registration.

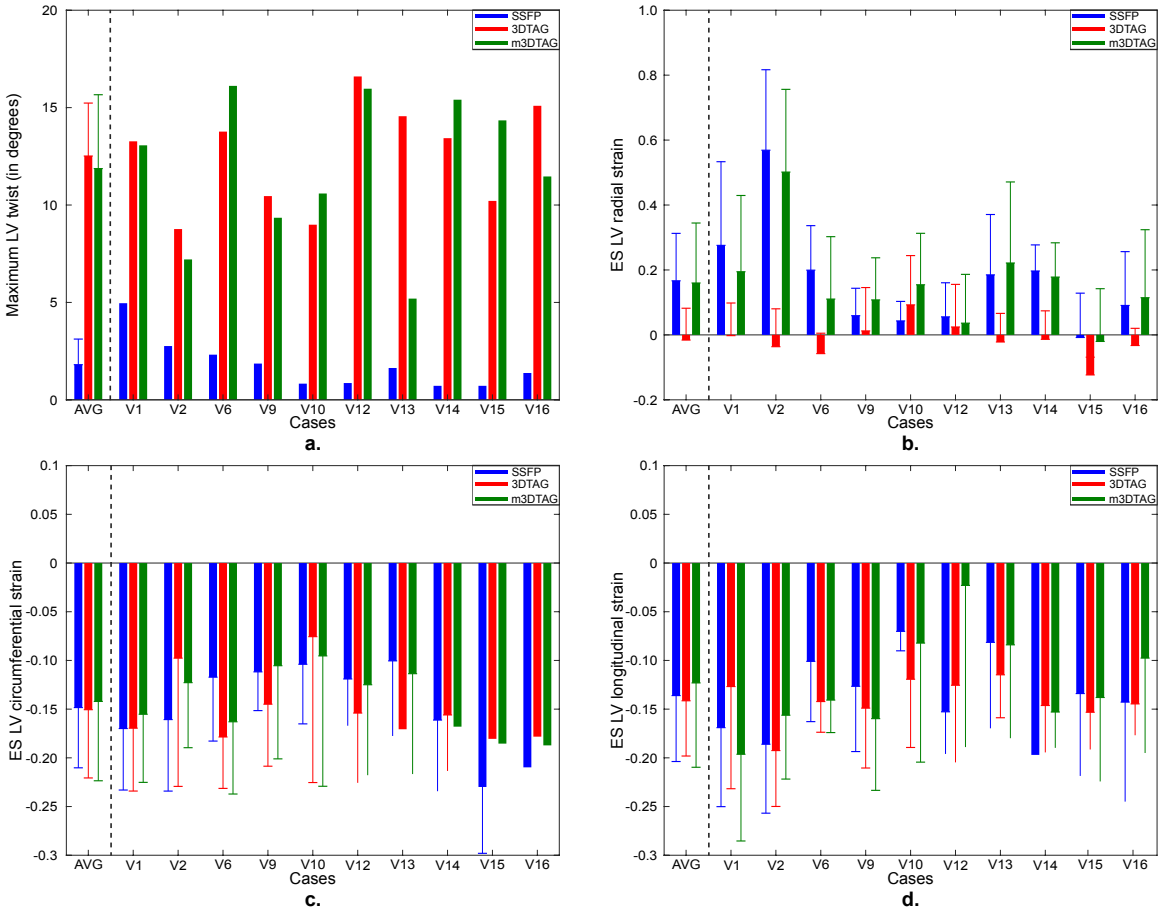

Figure 8 Results on Cardiac Motion Analysis Challenge data. Blue, red, and green bars represent SSFP, 3DTAG, and m3DTAG registrations, respectively. Maximum LV twist plotted for each volunteer with the average (AVG) over all volunteers (separated by a dashed line) included in the study (a). m3DTAG registration performs closer to 3DTAG registration in terms of LV twist quantification while SSFP yields comparably lower LV twist. End-systolic radial (b), circumferential (c) and longitudinal (d) strains are also represented for each volunteer with the averaged values (AVG) over all volunteers separated by a dashed line. In terms of radial strain quantification, compared to 3DTAG registration, there is a significant improvement on average when m3DTAG images are used. For the circumferential and longitudinal strains, SSFP and 3DTAG perform equally while m3DTAG images slightly underestimate the average values.

4. Discussion

In this study, we have proposed to combine the advantageous features of two imaging modalities: cine and 3DTAG CMR. This technique allowed us to obtain the global shape information from the cine MR images while the regional deformation is acquired from the tagged data.

The performance of the m3DTAG registration and the acquired myocardial deformation measures are strongly dependent on the mask, and by that the way we temporally interpolate the displacement fields from SSFP registration. The linear interpolation scheme utilized here could be improved by using higher order temporal functions to get a more accurate deformation estimate.

The error as function of background intensities for these LV twist and Green-Lagrange ES strain reveals that m3DTAG registration performs similar to SSFP registration as

image background intensity gets closer to the limits of the intensity range utilized, which can be explained with the higher image contrast between LV wall and the image background. Likewise, assigning image background intensity values close to average image intensity results in a decrease in image contrast around LV wall, hence, the m3DTAG registration performs closer to 3DTAG registration. Although we have observed a clear change in LV twist and radial strain errors for varying image background intensity, the errors in circumferential and longitudinal strain components stayed in the same range as SSFP image tracking error. Therefore, we defined the "optimal" image background intensity using the summation of normalized absolute error (%) in LV twist and radial strain component. The FEM-based image registration technique utilized here can be further improved by applying different weighting terms for the errors related to cine and 3DTAG registrations owing to the reverse trend in the change in LV twist and radial strain errors for varying image background intensity.

After determining the optimal background intensity, we first validated our joint analysis technique on the Cardiac Motion Tracking Challenge data (Tobon-Gomez et al., 2013) before presenting the strain and twist analysis results. The markers error computation is based on the manually tracked landmarks over 3DTAG. It was previously shown that FEM-based registration performs quite satisfactory in terms of markers errors for SSFP and 3DTAG image analysis (Genet et al., 2018). For all the cases, except V15, m3DTAG registration performs better than SSFP images in terms of markers error while it is slightly worse than 3DTAG images for most of the cases. The averaged errors presented by the first two groups of bar plots in Figure 4 reveal that markers error for m3DTAG registration stays in the error range that the challenge contributors have, proving the performance of our joint analysis technique. Nevertheless, it is interesting to see that the markers error is generally larger with m3DTAG compared to 3DTAG, despite radial strains appearing in a more physiological range. For instance, for volunteers V15 and V16, 3DTAG yields lower markers error than m3DTAG while producing negative radial strain whereas strains obtained from m3DTAG are more physiological. One reason may be that the markers were manually positioned on the images for the challenge, which contain a bias due to low resolution and SNR as established in (Berberoğlu et al., 2021). Consequently, these markers might not provide accurate ground truth for the actual tissue motion.

The combined approach of m3DTAG registration leverages the lack of capability to track LV twist of SSFP registration and outperforms 3DTAG image registration in the assessment of radial strain. In terms of circumferential and longitudinal strain components, we do not observe a significant difference for any image type. We performed the same study on human dataset, and analyzed maximum LV twist and ES strain components for SSFP, 3DTAG and m3DTAG registrations, and observed the same trend in both performance metrics. We further performed pairwise t-test on m3DTAG images in comparison to SSFP and 3DTAG, for both the porcine and human datasets to find out if the difference between registration results is systematic or random. For both porcine and human datasets, we did not observe a statistically significant difference for circumferential and longitudinal strain components, as expected. For the porcine data, we found statistically significant differences in radial strain component both for the SSFP and 3DTAG registrations in comparison to m3DTAG, which can be related to the shift between the means of two datasets. The bias in radial strain estimation is systematic and can be attributed to the tracking method itself. Although for the volunteer dataset, we have higher p-values for the radial

strain, it does not mean that there is no bias in the analysis results; this might be due to the random error component caused by the variational slice misalignment.

In order to investigate the agreement between SSFP, 3DTAG and m3DTAG registrations, we performed a Bland-Altman analysis for the porcine dataset, using the optimal background intensity. Similar to Figure 2, m3DTAG performance was assessed for LV twist and strain quantification with respect to 3DTAG and SSFP registration, respectively. In terms of the circumferential and longitudinal strain components, the mean differences obtained from comparing m3DTAG and 3DTAG with SSFP are close to each other, that supports our findings stated above. For LV twist, however, m3DTAG registration yields a mean difference closer to zero and smaller than 3DTAG registration. The superiority of m3DTAG registration over 3DTAG for the radial strain quantification is shown by a smaller absolute mean error.

Regarding the human datasets, it appears that quite low ES radial strain is measured even for SSFP images, that might have several underlying reasons: The FEM-based image registration technique is dependent on the segmentation and the image quality. The tracking performance drastically decreases in case the segmentation covers structures other than the ventricular wall. As mentioned in Section 2.1, we had to exclude five volunteer datasets due to slice misalignment. Moreover, the performance of m3DTAG registration in capturing the global shape information is correlated with SSFP registration. Any improper SSFP registration results in masking inaccurately of 3DTAG images, potentially including the structures outside the ventricle. Hence, m3DTAG registration performance decreases drastically if SSFP registration is not good enough. Despite the low radial strains from SSFP and m3DTAG registrations found in the human datasets, we still make the point; the m3DTAG images yield better radial strain estimation compared to 3DTAG only while being superior to SSFP registration in terms of twist quantification.

In order to improve the cardiac motion quantification, several techniques have been proposed to combine the tagged and untagged images (Shi et al., 2012; Tobon-Gomez et al., 2013). Recent studies on this area focus on the improvement of current techniques that allow for the quantification of the regional and global ventricular properties on a single scan, e.g., SubTag SSFP (Schrauben et al., 2018). This method allows for combining the assessment of both the ventricular function and more accurate regional strain in a single scan, although it still suffers from assessing the segmental heterogeneity in strain distribution.

5. Conclusion

This study shows that combined processing of cine and 3DTAG images provides better quantification of LV deformation as either data source alone. m3DTAG images yield better radial strain estimation compared to 3DTAG only while being superior to SSFP registration in terms of twist quantification. Moreover, performance of the FEM-based image registration on m3DTAG images is comparable to the benchmark techniques in terms of manually tracked markers error while yielding more physiological myocardial deformation measures.

Declaration of Competing Interest

The authors declare that they have no known competing financial interests or personal relationships that could have appeared to influence the work reported in this paper.

CRediT authorship contribution statement

Ezgi Berberoglu: Conceptualization, Formal analysis, Investigation, Methodology, Software, Validation, Visualization, Writing - original draft. **Christian T. Stoeck:** Conceptualization, Funding acquisition, Investigation, Methodology, Project administration, Resources, Supervision, Validation, Visualization, Writing - review & editing. **Sebastian Kozerke:** Conceptualization, Funding acquisition, Investigation, Methodology, Project administration, Resources, Supervision, Validation, Visualization, Writing - review & editing. **Martin Genet:** Conceptualization, Funding acquisition, Investigation, Methodology, Project administration, Software, Resources, Supervision, Validation, Visualization, Writing - review & editing.

Acknowledgement

The authors acknowledge funding of the Swiss National Science Foundation (SNF) Research Grants Nr. CR23I3166485 and PZ00P2174144, as well as of the French National Research Agency (ANR) Research Grant Nr. ANR-10-EQPX-37.

References

Abraham,T.P. and Nishimura,R.A., 2001. Myocardial strain: Can we finally measure contractility? Journal of the American College of Cardiology pp. 731–734. doi:10.1016/S0735-1097(00)01173-6.

Alfakih,K., Reid,S., Jones,T. and Sivananthan,M., 2004. Assessment of ventricular function and mass by cardiac magnetic resonance imaging. European Radiology 14(10), pp. 1813–1822. doi:10.1007/s00330-004-2387-0.

Augustine,D., Lewandowski,A.J., Lazdam,M., Rai,A., Francis,J., Myerson,S., Noble,A., Becher,H., Neubauer,S., Petersen,S.E. and Leeson,P., 2013. Global and regional left ventricular myocardial deformation measures by magnetic resonance feature tracking in healthy volunteers: Comparison with tagging and relevance of gender. Journal of Cardiovascular Magnetic Resonance. doi:10.1186/1532-429X-15-8.

Axel,L. and Dougherty,L., 1989. Heart wall motion: Improved method for spatial modulation of magnetization for MR imaging. Radiology. doi:10.1148/radiology.172.2.2748813.

Barkhausen,J., Ruehm,S.G., Goyen,M., Buck,T., Laub,G. and Debatin,J.F., 2001. MR evaluation of ventricular function: True fast imaging with steady-state precession versus fast low-angle shot cine MR imaging: Feasibility study. Radiology. doi:10.1148/radiology.219.1.r01ap12264.

Berberoğlu,E., Stoeck,C., Moireau,P., Kozerke,S. and Genet,M., 2019. Validation of Finite Element Image Registration-based Cardiac Strain Estimation from Magnetic Resonance Images. PAMM. doi:10.1002/pamm.201900418.

Berberoğlu,E., Stoeck,C.T., Moireau,P., Kozerke,S. and Genet,M., 2021. In-silico study of accuracy and precision of left-ventricular strain quantification from 3D tagged MRI. PloS one 16(11), p. e0258965. doi:10.1371/journal.pone.0258965.

Bilchick,K.C., Kuruvilla,S., Hamirani,Y.S., Ramachandran,R., Clarke,S.A., Parker,K.M., Stukenborg,G.J., Mason,P., Ferguson,J.D., Moorman,J.R., Malhotra,R., Mangrum,J.M., Darby,A.E., Dimarco,J., Holmes,J.W., Salerno,M., Kramer,C.M. and Epstein,F.H., 2014. Impact of mechanical activation, scar, and electrical timing on cardiac resynchronization therapy response and clinical outcomes. Journal of the American College of Cardiology 63(16), pp. 1657–1666. doi:10.1016/j.jacc.2014.02.533.

Bogaert,J. and Rademakers,F.E., 2001. Regional nonuniformity of normal adult human left ventricle. American journal of physiology. Heart and circulatory physiology 280(2), pp. H610-20.

Bohs,L.N., Geiman,B.J., Anderson,M.E., Gebhart,S.C. and Trahey,G.E., 2000. Speckle tracking for multi-dimensional flow estimation. Ultrasonics. doi:10.1016/S0041-624X(99)00182-1.

Castellanos,D.A., Škardová,K., Bhattaru,A., Berberoglu,E., Greil,G., Tandon,A., Dillenbeck,J., Burkhardt,B., Hussain,T., Genet,M. and Chabiniok,R., 2021. Left Ventricular Torsion Obtained Using Equilibrated Warping in Patients with Repaired Tetralogy of Fallot. Pediatric Cardiology 42(6), pp. 1275–1283. doi:10.1007/s00246-021-02608-y.

Castillo,E., Lima,J.A.C. and Bluemke,D.A., 2003. Regional Myocardial Function: Advances in MR Imaging and Analysis. Radiographics. doi:10.1148/rg.23si035512.

Claire,D., Hild,F. and Roux,S., 2004. A finite element formulation to identify damage fields: The equilibrium gap method. International Journal for Numerical Methods in Engineering. doi:10.1002/nme.1057.

Collins,J.D., 2015. Global and regional functional assessment of ischemic heart disease with cardiac MR imaging. Radiologic Clinics of North America. doi:10.1016/j.rcl.2014.11.001.
Cowan,B.R., Peereboom,S.M., Greiser,A., Guehring,J. and Young,A.A., 2015. Image Feature Determinants of Global and Segmental Circumferential Ventricular Strain from Cine CMR. JACC: Cardiovascular Imaging. doi:10.1016/j.jcmg.2014.10.005.
Fischer,S.E., McKinnon,G.C., Maier,S.E. and Boesiger,P., 1993. Improved myocardial tagging contrast. Magnetic Resonance in Medicine. doi:10.1002/mrm.1910300207.
Fischer,S.E., McKinnon,G.C., Scheidegger,M.B., Prins,W., Meier,D. and Boesiger,P., 1994. True myocardial motion tracking. Magnetic Resonance in Medicine. doi:10.1002/mrm.1910310409.
Friedberg,M.K. and Mertens,L., 2009. Tissue velocities, strain, and strain rate for echocardiographic assessment of ventricular function in congenital heart disease. European Journal of Echocardiography. doi:10.1093/ejechocard/jep045.
Genet,M., Lee,L.C., Nguyen,R., Haraldsson,H., Acevedo-Bolton,G., Zhang,Z., Ge,L., Ordovas,K., Kozerke,S. and Guccione,J.M., 2014. Distribution of normal human left ventricular myofiber stress at end diastole and end systole: a target for in silico design of heart failure treatments. Journal of Applied Physiology 117(2), pp. 142–152. doi:10.1152/japplphysiol.00255.2014.
Genet,M., Chuan Lee,L., Ge,L., Acevedo-Bolton,G., Jeung,N., Martin,A., Cambronero,N., Boyle,A., Yeghiazarians,Y., Kozerke,S. and Guccione,J.M., 2015. A Novel Method for Quantifying Smooth Regional Variations in Myocardial Contractility Within an Infarcted Human Left Ventricle Based on Delay-Enhanced Magnetic Resonance Imaging. Journal of Biomechanical Engineering. doi:10.1115/1.4030667.
Genet,M., Stoeck,C.T., Deuster,C. Von, Lee,L.C. and Kozerke,S., 2018. Equilibrated Warping: Finite Element Image Registration with Finite Strain Equilibrium Gap Regularization. Medical Image Analysis 50, pp. 1–22. doi:10.1016/j.media.2018.07.007.
Geuzaine,C. and Remacle,J.-F., 2009. Gmsh: a Three-Dimensional Finite Element Mesh Generator with Built-in Pre- and Post-Processing. Facilities. Int. J. Numer. Meth. Eng.
Haggerty,C.M., Kramer,S.P., Binkley,C.M., Powell,D.K., Mattingly,A.C., Charnigo,R., Epstein,F.H. and Fornwalt,B.K., 2013. Reproducibility of cine displacement encoding with stimulated echoes (DENSE) cardiovascular magnetic resonance for measuring left ventricular strains, torsion, and synchrony in mice. Journal of cardiovascular magnetic resonance : official journal of the Society for Cardiovascular Magnetic Resonance 15(1), p. 71. doi:10.1186/1532-429X-15-71.
Haggerty,C.M., Kramer,S.P., Skrinjar,O., Binkley,C.M., Powell,D.K., Mattingly,A.C., Epstein,F.H. and Fornwalt,B.K., 2014. Quantification of left ventricular volumes, mass, and ejection fraction using cine displacement encoding with stimulated echoes (DENSE) MRI. Journal of magnetic resonance imaging : JMRI 40(2), pp. 398–406. doi:10.1002/jmri.24350.
Hasselberg,N.E., Haugaa,K.H., Sarvari,S.I., Gullestad,L., Andreassen,A.K., Smiseth,O.A. and Edvardsen,T., 2015. Left ventricular global longitudinal strain is associated with exercise capacity in failing hearts with preserved and reduced ejection fraction. European heart journal cardiovascular Imaging. doi:10.1093/ehjci/jeu277.
Hor,K.N., Gottliebson,W.M., Carson,C., Wash,E., Cnota,J., Fleck,R., Wansapura,J., Klimeczek,P., Al-Khalidi,H.R., Chung,E.S., Benson,D.W. and Mazur,W., 2010.

Comparison of Magnetic Resonance Feature Tracking for Strain Calculation With Harmonic Phase Imaging Analysis. JACC: Cardiovascular Imaging. doi:10.1016/j.jcmg.2009.11.006.
Huang,J., Yan,Z.N., Fan,L., Rui,Y.F. and Song,X.T., 2017. Left ventricular systolic function changes in hypertrophic cardiomyopathy patients detected by the strain of different myocardium layers and longitudinal rotation. BMC Cardiovascular Disorders. doi:10.1186/s12872-017-0651-x.
Hunter,W.C. and Zerhouni,E.A., 2012. Imaging Distinct Points in Left Ventricular Myocardium to Study Regional Wall Deformation. in. doi:10.1007/978-3-642-83413-4_10.
Ibrahim,E.-S.H., 2011. Myocardial tagging by Cardiovascular Magnetic Resonance: evolution of techniques--pulse sequences, analysis algorithms, and applications. Journal of Cardiovascular Magnetic Resonance 13(1), p. 36. doi:10.1186/1532-429X-13-36.
Kim,D., Gilson,W.D., Kramer,C.M. and Epstein,F.H., 2004. Myocardial Tissue Tracking with Two-dimensional Cine Displacement-encoded MR Imaging: Development and Initial Evaluation. Radiology. doi:10.1148/radiol.2303021213.
Lee,L.C. and Genet,M., 2019. Validation of Equilibrated Warping—Image Registration with Mechanical Regularization—On 3D Ultrasound Images. inLecture Notes in Computer Science (including subseries Lecture Notes in Artificial Intelligence and Lecture Notes in Bioinformatics). doi:10.1007/978-3-030-21949-9_36.
Makram,A.W., Khalifa,A.M., El-Rewaidy,H., Fahmy,A.S. and Ibrahim,E.S.H., 2016. Assessment of cardiac mass from tagged magnetic resonance images. Japanese Journal of Radiology 34(2), pp. 158–165. doi:10.1007/s11604-015-0504-4.
Moore,C.C., Lugo-Olivieri,C.H., McVeigh,E.R. and Zerhouni,E.A., 2000. Three-dimensional systolic strain patterns in the normal human left ventricle: Characterization with tagged MR imaging. Radiology. doi:10.1148/radiology.214.2.r00fe17453.
Morton,G., Schuster,A., Jogiya,R., Kutty,S., Beerbaum,P. and Nagel,E., 2012. Inter-study reproducibility of cardiovascular magnetic resonance myocardial feature tracking. Journal of Cardiovascular Magnetic Resonance. doi:10.1186/1532-429X-14-43.
Nagueh,S.F., Bachinski,L.L., Meyer,D., Hill,R., Zoghbi,W.A., Tam,J.W., Quiñones,M.A., Roberts,R. and Marian,A.J., 2001. Tissue Doppler imaging consistently detects myocardial abnormalities in patients with hypertrophic cardiomyopathy and provides a novel means for an early diagnosis before and independently of hypertrophy. Circulation 104(2), pp. 128–130. doi:10.1161/01.CIR.104.2.128.
Ng,A.C.T., Delgado,V., Bertini,M., Antoni,M.L., Van Bommel,R.J., Van Rijnsoever,E.P.M., Van Der Kley,F., Ewe,S.H., Witkowski,T., Auger,D., Nucifora,G., Schuijf,J.D., Poldermans,D., Leung,D.Y., Schalij,M.J. and Bax,J.J., 2011. Alterations in multidirectional myocardial functions in patients with aortic stenosis and preserved ejection fraction: A two-dimensional speckle tracking analysis. European Heart Journal 32(12), pp. 1542–1550. doi:10.1093/eurheartj/ehr084.
Padiyath,A., Gribben,P., Abraham,J.R., Li,L., Rangamani,S., Schuster,A., Danford,D.A., Pedrizzetti,G. and Kutty,S., 2013. Echocardiography and cardiac magnetic resonance-based feature tracking in the assessment of myocardial mechanics in tetralogy of fallot: An intermodality comparison. Echocardiography. doi:10.1111/echo.12016.

Pedrizzetti,G., Gottliebson,W.M., Hor,K.N., Benson,W., Baumann,R., Taylor,M., Mazur,W. and Tonti,G., 2011. Magnetic Resonance Derived Myocardial Strain Assessment Using Feature Tracking. Journal of Visualized Experiments. doi:10.3791/2356.
Pereles,F.S., Kapoor,V., Carr,J.C., Simonetti,O.P., Krupinski,E.A., Baskaran,V. and Finn,J.P., 2001. Usefulness of segmented trueFISP cardiac pulse sequence in evaluation of congenital and acquired adult cardiac abnormalities. American Journal of Roentgenology. doi:10.2214/ajr.177.5.1771155.
Plein,S., Bloomer,T.N., Ridgway,J.P., Jones,T.R., Bainbridge,G.J. and Sivananthan,M.U., 2001. Steady-state free precession magnetic resonance imaging of the heart: Comparison with segmented K-space gradient-echo imaging. Journal of Magnetic Resonance Imaging. doi:10.1002/jmri.1178.
Rademakers,F.E. and Bogaert,J., 1997. Left ventricular myocardial tagging. The International Journal of Cardiac Imaging 13(3), pp. 233–245. doi:10.1023/A:1005731100601.
Rutz,A.K., Ryf,S., Plein,S., Boesiger,P. and Kozerke,S., 2008. Accelerated whole-heart 3D CSPAMM for myocardial motion quantification. Magnetic Resonance in Medicine. doi:10.1002/mrm.21363.
Schrauben,E.M., Cowan,B.R., Greiser,A. and Young,A.A., 2018. Left ventricular function and regional strain with subtly-tagged steady-state free precession feature tracking. Journal of Magnetic Resonance Imaging 47(3), pp. 787–797. doi:10.1002/jmri.25819.
Schuster,A., Kutty,S., Padiyath,A., Parish,V., Gribben,P., Danford,D.A., Makowski,M.R., Bigalke,B., Beerbaum,P. and Nagel,E., 2011. Cardiovascular magnetic resonance myocardial feature tracking detects quantitative wall motion during dobutamine stress. Journal of Cardiovascular Magnetic Resonance. doi:10.1186/1532-429X-13-58.
Schuster,A., Paul,M., Bettencourt,N., Morton,G., Chiribiri,A., Ishida,M., Hussain,S., Jogiya,R., Kutty,S., Bigalke,B., Perera,D. and Nagel,E., 2013. Cardiovascular magnetic resonance myocardial feature tracking for quantitative viability assessment in ischemic cardiomyopathy. International Journal of Cardiology. doi:10.1016/j.ijcard.2011.10.137.
Schuster,A., Morton,G., Hussain,S.T., Jogiya,R., Kutty,S., Asrress,K.N., Makowski,M.R., Bigalke,B., Perera,D., Beerbaum,P. and Nagel,E., 2013. The intra-observer reproducibility of cardiovascular magnetic resonance myocardial feature tracking strain assessment is independent of field strength. European Journal of Radiology. doi:10.1016/j.ejrad.2012.11.012.
Serri,K., Reant,P., Lafitte,M., Berhouet,M., Le Bouffos,V., Roudaut,R. and Lafitte,S., 2006. Global and regional myocardial function quantification by two-dimensional strain: Application in hypertrophic cardiomyopathy. Journal of the American College of Cardiology. doi:10.1016/j.jacc.2005.10.061.
Shi,W., Zhuang,X., Wang,H., Duckett,S., Luong,D.V.N., Tobon-Gomez,C., Tung,K., Edwards,P.J., Rhode,K.S., Razavi,R.S., Ourselin,S. and Rueckert,D., 2012. A comprehensive cardiac motion estimation framework using both untagged and 3-D tagged MR images based on nonrigid registration. IEEE Transactions on Medical Imaging. doi:10.1109/TMI.2012.2188104.
Smiseth,O.A., Torp,H., Opdahl,A., Haugaa,K.H. and Urheim,S., 2016. Myocardial strain imaging: How useful is it in clinical decision making? European Heart Journal. doi:10.1093/eurheartj/ehv529.
Stoeck,C.T., Manka,R., Boesiger,P. and Kozerke,S., 2012. Undersampled Cine 3D

tagging for rapid assessment of cardiac motion. Journal of Cardiovascular Magnetic Resonance. doi:10.1186/1532-429X-14-60.
Stoeck,C.T., von Deuster,C., Fuetterer,M., Polacin,M., Waschkies,C.F., van Gorkum,R.J.H., Kron,M., Fleischmann,T., Cesarovic,N., Weisskopf,M. and Kozerke,S., 2021. Cardiovascular magnetic resonance imaging of functional and microstructural changes of the heart in a longitudinal pig model of acute to chronic myocardial infarction. Journal of Cardiovascular Magnetic Resonance 23(1), pp. 1–14. doi:10.1186/s12968-021-00794-5.
Stuber,M., Scheidegger,M.B., Fischer,S.E., Nagel,E., Steinemann,F., Hess,O.M. and Boesiger,P., 1999. Alterations in the local myocardial motion pattern in patients suffering from pressure overload due to aortic stenosis. Circulation. doi:10.1161/01.CIR.100.4.361.
Sutherland,G.R., Stewart,M.J., Groundstroem,K.W.E., Moran,C.M., Fleming,A., Guell-Peris,F.J., Riemersma,R.A., Fenn,L.N., Fox,K.A.A. and McDicken,W.N., 1994. Color Doppler Myocardial Imaging: A New Technique for the Assessment of Myocardial function. Journal of the American Society of Echocardiography. doi:10.1016/S0894-7317(14)80001-1.
Tobon-Gomez,C. *et al.*, 2013. Benchmarking framework for myocardial tracking and deformation algorithms: An open access database. Medical Image Analysis 17(6), pp. 632–648. doi:10.1016/j.media.2013.03.008.
Wu,L., Germans,T., Güçlü,A., Heymans,M.W., Allaart,C.P. and van Rossum,A.C., 2014. Feature tracking compared with tissue tagging measurements of segmental strain by cardiovascular magnetic resonance. Journal of cardiovascular magnetic resonance : official journal of the Society for Cardiovascular Magnetic Resonance 16(1), p. 10. doi:10.1186/1532-429X-16-10.
Young,A.A., Kramer,C.M., Ferrari,V.A., Axel,L. and Reichek,N., 1994. Three-dimensional left ventricular deformation in hypertrophic cardiomyopathy. Circulation 90(2), pp. 854–867. doi:10.1161/01.CIR.90.2.854.
Zerhouni,E.A., Parish,D.M., Rogers,W.J., Yang,A. and Shapiro,E.P., 1988. Human heart: tagging with MR imaging--a method for noninvasive assessment of myocardial motion. Radiology 169(1), pp. 59–63. doi:10.1148/radiology.169.1.3420283.